Technical University of Denmark

Indentation of pressurized viscoplastic polymer spherical shells

Tvergaard, Viggo; Needleman, A.

Link back to DTU Orbit

DTU Library
Technical Information Center of Denmark

Indentation of pressurized viscoplastic polymer spherical shells

V. Tvergaard[a], A. Needleman[b,*]

[a]*Department of Mechanical Engineering, The Technical University of Denmark, Lyngby, Denmark*
[b]*Department of Materials Science & Engineering, Texas A&M University, College Station, TX 77843 USA*

Abstract

The indentation response of polymer spherical shells is investigated. Finite deformation analyses are carried out with the polymer characterized as a viscoelastic/viscoplastic solid. Both pressurized and unpressurized shells are considered. Attention is restricted to axisymmetric deformations with a conical indenter. The response is analyzed for various values of the shell thickness to radius ratio and various values of the internal pressure. Two sets of material parameters are considered: one set having network stiffening at a moderate strain and the other having no network stiffening until very large strains are attained. The transition from an indentation type mode of deformation to a structural mode of deformation involving bending that occurs as the indentation depth increases is studied. The results show the effects of shell thickness, internal pressure and polymer constitutive characterization on this transition and on the deformation modes in each of these regimes.

Keywords: Indentation; viscoplasticity; polymer; pressurized shell

1. Introduction

There has recently been a great deal of interest in measuring mechanical properties by indentation of shells under internal pressure. Thus, Vella et al. (2012a) have studied both polymeric capsules and yeast cells, and Milani et al. (2011) have studied the cell wall in living shoot apical meristems (SAMs), which are highly organized structures that contain the plant stem cells. For the cells the experiments are based on microindentation techniques, using atomic force microscopy (AFM). Vella et al. (2012a) also analyze the relation between indentation depth, indenter force and internal pressure, using linear shallow shell theory, or nonlinear shell theory in cases where the indentation depth is much larger than the shell thickness. Kol et al. (2006) used indentation to investigate the mechanical properties of a leukemia virus particle and carried out elastic finite element calculations to use in conjunction with the experimental measurements to quantify virus particle stiffness. Zelenskaya et al. (2005) used atomic force microscopy together with indentation analyses to understand the mechanical behavior of cochlear hair cells.

---

*

Email address: `needle.tamu@gmail.com` (A. Needleman)

Ogbonna and Needleman (2011) carried out a numerical study for indentation of thick-walled elastic spherical shells using finite strain elastic theory to be able to represent the geometry changes during bending, as well as the initial indentation response, where bending is not yet noticeable. A variety of studies have been carried out investigating the indentation of thin shells, e.g. Fitch and Budiansky (1970); Vaziri and Mahadevan (2008); Vella et al. (2012a,b); Nasto and Reis (2014), with attention directed to the emergence of non-axisymmetric deformation mode and with the focus on elastic material response. Here, we focus on indentation of relatively thick spherical shell and confine attention to axisymmetric deformations. We carry out our analyses using full finite deformation kinematics and a material constitutive relation including viscoelastic and viscoplastic material response.

The constitutive relation used for the finite strain behavior of the polymers is mainly adopted from Wu and Van der Giessen (1996) and models proposed by Boyce et al. (1988) and Boyce et al. (1990). The indentation analyses first considered material parameters that give a reasonable approximation of tensile tests for high-density polyethylene, and subsequently indentation was analyzed for a number of different parameter sets that represent other polymers. In the analyses the effect of viscoelasticity is modeled following discussions by Anand and Ames (2006). This material model was used by Tvergaard and Needleman (2011, 2012) in full 3D numerical analyses of indentation into a polymer half-space by conical and pyramidal indenters.

For metals it is well known that the hardness is about three times the yield strength (Johnson (1970, 1985)), but such high hardness values are not found in the analyses of polymer indentation. Recently, Needleman et al. (2015) have studied indentation of elastically soft or plastically compressible solids, and these results show that a hardness around 1.1 times the yield stress is consistent with a polymer having Youngs modulus around 19 times the yield stress. Plastic analyses of shell indentation aimed at structural applications have been carried out, including the work of Morris and Calladine (1971) on indentation of cylindrical shells using upper bound analyses. Analyses of shell plastic indentation aimed at structural applications include the work of Morris and Calladine (1971) on indentation of cylindrical shells. They used their results to delineate between an elasticity dominated regime where snap-through occurs and a plasticity dominated regime where it does not occur.

The indentation studies of Tvergaard and Needleman (2011, 2012) also considered the spherical cavity model, which was suggested by Bishop et al. (1945) as an alternative approach to elastic-plastic indentation, and later carefully discussed by Johnson Johnson (1970, 1985). It was found that also for the polymers this simpler 1D model with spherical symmetry gives a good approximation of the indentation hardness for indentation into a half-space.

A basic question for indentation into shells is the extent to which the indentation hardness (indentation force/some measure of contact area) provides a measure of a material property or reflects the overall structural response, including the shell geometry and the internal pressure (if any).

In the present paper we confine attention to the indentation of spherical shell by conical indenters. The cases analyzed include various thickness to radius ratios and various values of internal pressure. Also, two sets of the material parameters from Tvergaard and Needleman

2

(2012) are used in the calculations: one, termed material G has network stiffening come into play at a strain of about 0.3 while the other termed material A does not undergo network stiffening until very large strains.

For sufficiently small indentation depths, we expect the indentation response to be the same as for a half-space. For larger indentation depths, the overall structural response of the shell, as well as the material response, comes into play. The effects of the two constitutive characterizations and of the value of the prescribed internal pressure on the indentation responses in these two regimes and the transition between them is investigated.

2. Constitutive Relation

The constitutive relation used in the calculations is mainly adopted from Wu and Van der Giessen (1996) and is based on models proposed by Boyce and co-workers, see (Boyce et al., 1988, 1990; Arruda et al., 1993; Mulliken et. al., 2006). The specific formulation and implementation used in the calculations are those used in Tvergaard and Needleman (2011) where further details and additional references are given.

The rate of deformation tensor is written as

$$\boldsymbol{D} = \boldsymbol{D}^e + \boldsymbol{D}^{p1} + \boldsymbol{D}^{p2} \tag{1}$$

with

$$\boldsymbol{D}^e = \boldsymbol{K}^{-1} : \hat{\boldsymbol{\sigma}} \ , \ \boldsymbol{D}^{p1} = \dot{\gamma}^{p1} \boldsymbol{p}^{p1} \ , \ \boldsymbol{D}^{p2} = \dot{\gamma}^{p2} \boldsymbol{p}^{p2} \tag{2}$$

where $\boldsymbol{\sigma}$ is the Cauchy or true stress, a superposed ($\hat{\ }$) denotes the Jaumann rate and $\boldsymbol{K}$ is the isotropic tensor of moduli with elastic constants Young's modulus E and Poisson's ratio ν. The expression for $\boldsymbol{D}^e$ in Eq. (2) is a hypoelastic relation and is not, in general, a path independent hyperelastic relation. Attention here is confined to circumstances where the elastic strains remain relatively small.

The viscoplastic term, $\boldsymbol{D}^{p1}$, is given by

$$\boldsymbol{p}^{p1} = \frac{\boldsymbol{\sigma}' - \boldsymbol{b}'}{\sqrt{2}\tau} \quad , \quad \tau = \sqrt{\frac{1}{2}(\boldsymbol{\sigma}' - \boldsymbol{b}') : (\boldsymbol{\sigma}' - \boldsymbol{b}')} \tag{3}$$

with ( )$'$ denoting deviatoric quantities with, for example,

$$\boldsymbol{\sigma}' = \boldsymbol{\sigma} - \sigma_h \boldsymbol{I} \ , \ \sigma_h = \frac{1}{3}\text{tr}(\boldsymbol{\sigma}) \tag{4}$$

with $\boldsymbol{I}$ the identity tensor and tr( ) the trace of a tensor.

The scalar plastic strain rate $\dot{\gamma}^{p1}$ is given by

$$\dot{\gamma}^{p1} = \dot{\gamma}_0 \exp\left[-\frac{\Delta G}{kT}\left\{1 - \left(\frac{\tau}{s - \alpha(\text{tr}\boldsymbol{\sigma})/3}\right)^m\right\}\right] - \dot{\gamma}_0 \exp\left[-\frac{\Delta G}{kT}\right] \tag{5}$$

with the last term in Eq. (5) included so that $\dot{\gamma}^{p1} = 0$ when $\tau = 0$.

The material parameter s in Eq. (5) has the initial value s_0 and is taken to evolve as

$$\dot{s} = h\left(1 - \frac{s}{s_{ss}}\right)\dot{\gamma}^{p1} \tag{6}$$

The back stress $\boldsymbol{b}$ is given by Arruda et al. (1993),

$$\boldsymbol{b} = \frac{1}{3}C_R\sqrt{N}\frac{\beta_c}{\lambda_c}\boldsymbol{B} \tag{7}$$

where $\boldsymbol{B} = \boldsymbol{F} \cdot \boldsymbol{F}^T$, with $\boldsymbol{F}$ being the deformation gradient, and

$$\lambda_c^2 = \frac{1}{3}\text{tr}\boldsymbol{B} \quad , \quad \beta_c = \mathcal{L}^{-1}\left(\frac{\lambda_c}{\sqrt{N}}\right) \tag{8}$$

with

$$\mathcal{L}(x) = \coth(x) - \frac{1}{x} \tag{9}$$

The value of $\sqrt{N}$ defines a limit stretch such that when λ_c approaches $\sqrt{N}$ the hardening rate grows very large, modeling increased network stiffness.

In the manner of Anand and Ames (2006) we include a second term, here taken to be the term $\boldsymbol{D}^{p2}$ to model linear rate dependence via

$$\boldsymbol{p}^{p2} = [\boldsymbol{\sigma}' - \boldsymbol{b}' - \boldsymbol{c}'] \tag{10}$$

At $t = 0$, $\boldsymbol{c} = \boldsymbol{0}$ and we take the evolution equation for $\boldsymbol{c}$ to be

$$\hat{\boldsymbol{c}} = \mu^{p2}\boldsymbol{K} : \boldsymbol{D}^{p2} \tag{11}$$

where $\dot{\gamma}^{p2}$ and μ^{p2} are material constants, and $\dot{\gamma}^{p2}$ is

$$\dot{\gamma}^{p2} = \frac{1}{\nu^{p2}} \tag{12}$$

The inclusion of $\boldsymbol{D}^{p2}$ allows a rate dependent response at relatively small strains to be modeled. Due to this term the initial slope of a uniaxial stress-strain curve increases for increasing rate of deformation. The viscoplastic term $\boldsymbol{D}^{p1}$ will dominate at large strains.

Combining Eqs.(1) and (2) gives

$$\hat{\boldsymbol{\sigma}} = \boldsymbol{K} : \left[\boldsymbol{D} - \dot{\gamma}^{p1}\boldsymbol{p}^{p1} - \dot{\gamma}^{p2}\boldsymbol{p}^{p2}\right] \tag{13}$$

The calculations are carried out for two sets of material parameters, termed Material A and Material G in Tvergaard and Needleman (2012). For both materials Young's modulus and Poisson's ratio are taken to be $E = 760$ MPa and $\nu = 0.42$ and the viscoelasticity parameters in Eqs. (1) and (11) are $\dot{\gamma}^{p2} = 1/100(\text{MPa s})^{-1}$ and $\mu^{p2} = 1$. Also, $\rho = 960$ kg/m³, $m = 0.2$, $\dot{\gamma}_0 = 8.94\times10^3$ s^{-1}, $\Delta G = 3.744\times10^{-19}$ J, $\alpha = 0.08$ and $k = 1.3810^{-23}$ J/K, with the temperature $T = 298$ K . The remaining material parameters are given in Table 1. The homogeneous uniaxial compression stress-strain response of these two materials is shown in Fig. 1.

Table 1: Material parameters used in the calculations.

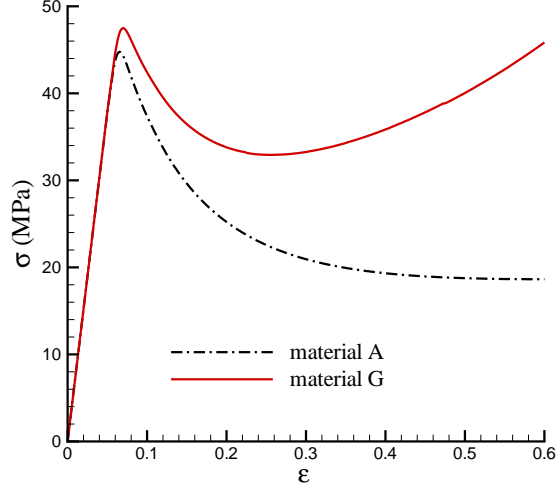| Material	h	s_0	s_{ss}	m	C_R	N
A	80.0	33.0	12.0	0.2	0.5	50.0
G	80.0	33.0	12.0	0.2	10.0	2.3

Figure 1: Homogeneous uniaxial compression stress-strain curves for materials A and G at $\dot{V}/L_0 = 1\mathrm{s}^{-1}$.

3. Problem formulation and numerical method

We consider a spherical shell indented by a sharp indenter, possibly after being subject to a prescribed internal pressure. Attention is restricted to axisymmetric deformations. The loading is applied in two phases: (i) the internal pressure p is increased monotonically until a specified pressure is reached; and (ii) the sphere is then indented along the axis of symmetry by a conical indenter (see Fig. 2). In the computations symmetry about the central plane is assumed, so that the results correspond to simultaneous indentation at two opposite poles of the shell.

The calculations are based on the dynamic principle of virtual work written as

$$\int_\Omega \tau^{ij}\delta E_{ij}\, dV + p\int_{S_p}\alpha^{ir} n_r \delta u_i\, dS = \int_\Omega \rho\frac{\partial^2 u^i}{\partial t^2}\delta u_i\, dV \tag{14}$$

with

$$E_{ij} = \frac{1}{2}(u_{i,j} + u_{j,i} + u^k_{,i}u_{k,j}) \tag{15}$$

$$\alpha^{ir} = \frac{1}{2}\epsilon^{ijk}\epsilon^{lmr}(g_{jl} + u_{j,l})(g_{km} + u_{k,m}) \tag{16}$$

5

where τ^{ij} are the contravariant components of Kirchhoff stress on the deformed convected coordinate net ($\tau^{ij} = J\sigma^{ij}$, with σ^{ij} being the contravariant components of the Cauchy stress and J the ratio of current to reference volume), n_r and u_j are the covariant components of the reference surface normal and displacement vectors, respectively, ρ is the mass density, g_{ij} are the covariant components of the reference metric tensor, $(\ )_{,i}$ denotes covariant differentiation in the reference frame, and Ω and S are the volume and surface of the body in the reference configuration. All field quantities are considered to be functions of convected coordinates, y^i, and time, t.
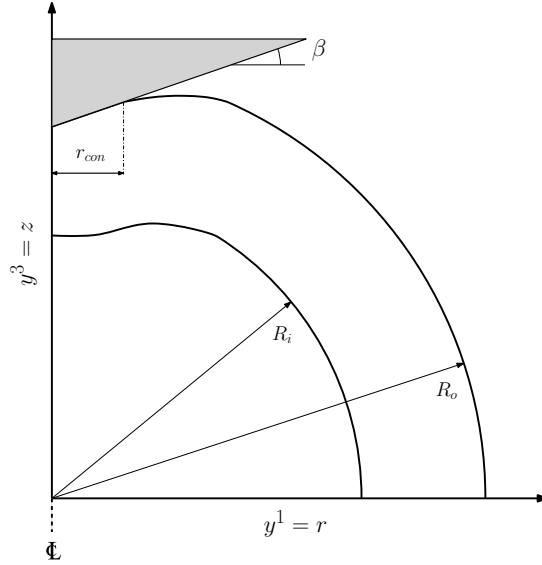

Figure 2: Sketch of the indentation boundary value problem.

During the indentation phase, the rate boundary conditions are

$$\dot{u}_3 = -\dot{h} \qquad \text{on} \quad S_{\text{contact}} \tag{17}$$

where h is the indentation depth, S_{contact} denotes the portion of the surface of the sphere in contact with the indenter, $(\dot{\ })$ denotes differentiation with respect to time and

$$\dot{h}(t) = \begin{cases} Vt/t_r & \text{for } t < t_r \\ V & \text{for } t > t_r \end{cases} \tag{18}$$

The indentation initial/boundary value problem is illustrated in Fig. 2. In all indentation calculations, the angle β is taken as $\beta = 19°$. Although, a deformed configuration is shown in Fig. 2, R_i and R_o are the initial, undeformed inner and outer radii, respectively. The shell thickness, denoted by ΔR is given by $\Delta R = R_o - R_i$. A polar coordinate system is used in the reference configuration with $y^1 = r$, $y^2 = \theta$ and $y^3 = z$. Since attention is restricted to axisymmetric deformations, all field quantities are independent of θ. The quantity r_{con} is the contact radius, defined as the largest distance in the deformed configuration from

6

the symmetry axis where the indenter and outer surface of the shell are in contact and $S_{\text{contact}} = \pi r_{\text{con}}^2$.

The finite element implementation uses eight node quadratic elements with four point Gauss integration except for the mass matrix where nine point Gauss integration is used.

4. Numerical results

4.1. Plane strain and axisymmetric compression

As seen in Fig. 1 both material A and material G undergo softening in homogeneous compression. The unique solution for a homogeneous material in both uniaxial compression and plane strain compression is a state of uniform stress and strain. Material G differs from material A in that it rehardens at a strain of ≈ 0.25 while material A does not reharden until very large strains have taken place.
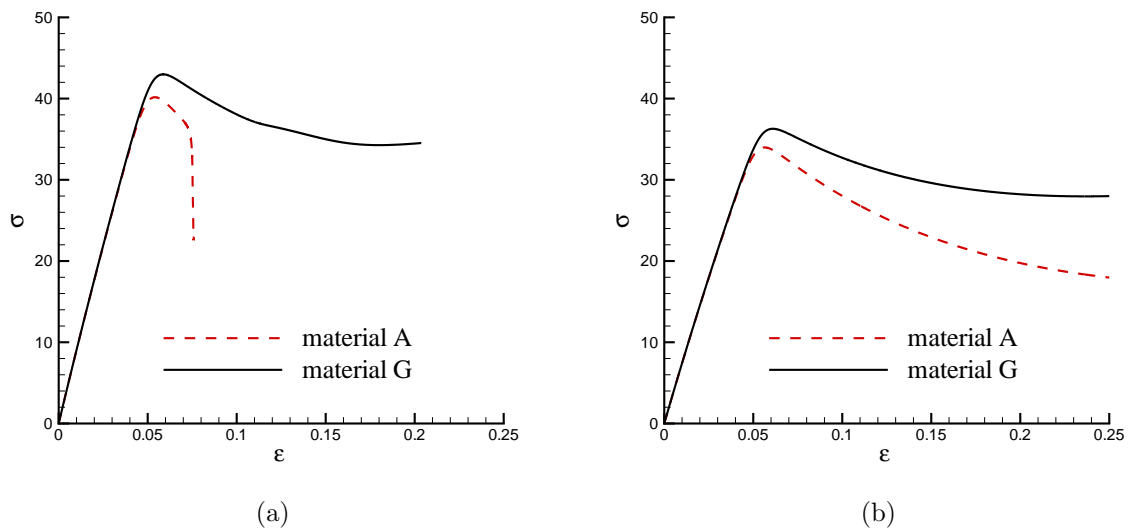

Figure 3: Stress-strain curves for materials A and G with an imperfection with $V/L_0 = 1\mathrm{s}^{-1}$. (a) Plane strain compression. (b) Axisymmetric compression.

As is well-known, softening promotes the localization of deformation. However, the propensity to form a localized deformation mode is very deformation state dependent. In particular, a plane strain state is readily susceptible to localization while axisymmetric states are quite resistant to localization, see e.g. Rice (1977). For rate dependent materials, an initial inhomogeneity is needed to trigger localization if it is to occur.

Calculations of plane strain and axisymmetric compression were carried out for materials A and G. An initial imperfection consisting of a value of s_0 of 0.9 times the value in the remainder of the specimen was prescribed in the element at the center of the specimen. The specimen has length $2L_0$, width $2w_0$ for plane strain compression and radius w_0 for
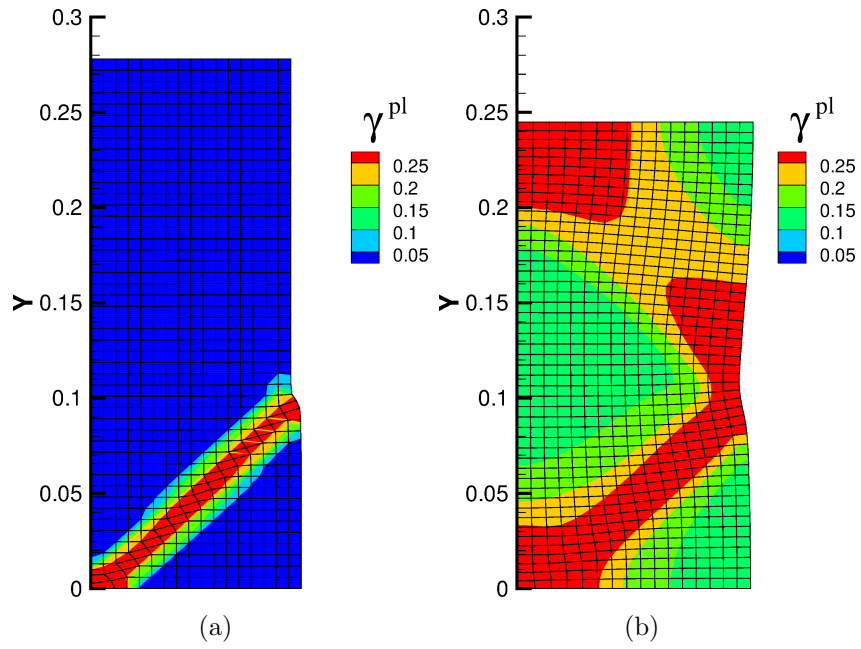
Figure 4: Contours of effective plastic strain in plane strain compression with $V/L_0 = 1\text{s}^{-1}$. (a) Material A at $\epsilon = 0.076$. (b) Material G at $\epsilon = 0.20$.
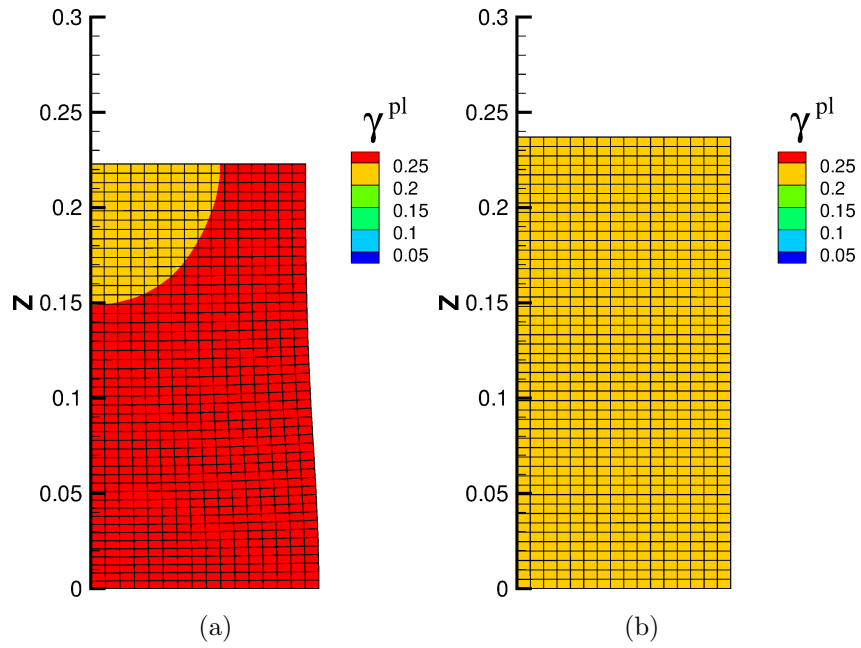

Figure 5: Contours of effective plastic strain in axisymmetric compression with $V/L_0 = 1\text{s}^{-1}$. (a) Material A at $\epsilon = 0.30$. (b) Material G at $\epsilon = 0.24$.

8

axisymmetric compression with $L_0/w_0 = 3$. The region $0 \leq y^1 \leq w_0$ and $0 \leq y^2 \leq L_0$ is analyzed. An imposed velocity $\dot{U}(t)$ is applied on $y^2 = L_0$ having a time variation of the form of Eq. (18) with $V/L_0 = 1$ s^{-1}, traction free conditions on $y^1 = w_0$ and symmetry conditions on the remaining boundaries of the region analyzed.

The computed stress-strain response is shown in Fig. 3(a) for plane strain compression and in Fig. 3(b) for axisymmetric compression. In plane strain compression, Fig. 3(a), material A undergoes a strong load drop at $\epsilon \approx 0.07$ whereas the stress-strain response for material G differs little from that for a homogeneous solid. On the other hand, in axisymmetric compression the response for neither material shows a strong load drop.

The deformation modes for materials A and G for plane strain compression are shown in Fig. 4. For material A the deformations show localization in a narrow band with a corresponding steep decay of the load. For material G the deformations show traces of an early attempt to localize, but this has been stopped at an early stage by network stiffening. For axisymmetric compression, Fig. 5, the deformations remain nearly homogeneous with no evidence of a localized deformation band.

The deformation state dependence of the the tendency for deformations to localize affects the shell indentation response, as will be seen subsequently.
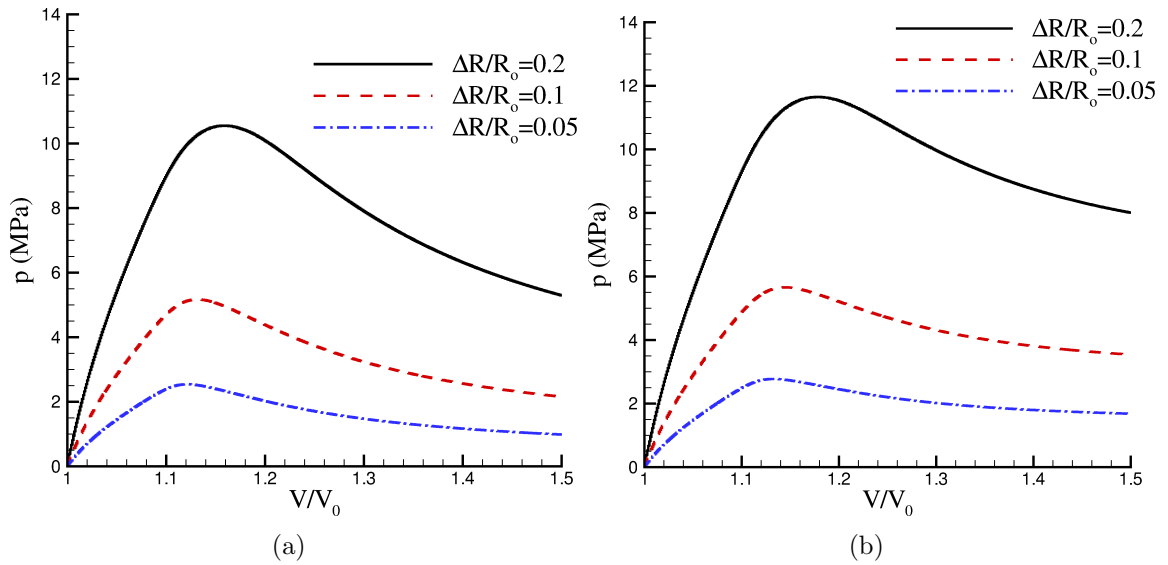
4.2. Spherical expansion

Figure 6: The pressure volume response for $\Delta R/R_o = 0.05, 0.1, 0.2$. (a) material A. (b) material G.

The pressure-volume response of materials A and G is shown in Fig. 6 for three values of shell thickness, $\Delta R/R_o = 0.05, 0.1, 0.2$. Here V is the current volume enclosed by the inner radius of the shell, V_0 is the corresponding initial volume and p is the pressure acting on the inner shell surface. In these calculation, the deformations constrained to be spherically symmetric by imposing spherically symmetric displacements on the inner shell surface. For

material A, the values of the maximum pressure are 2.5, 5.2 and 10.6 MPa, for $\Delta R/R_o = 0.05, 0.1, 0.2$, respectively, while the corresponding pressure maximum values are 2.8, 5.7 and 11.6 MPa for material G. For both material A and material G, the variation of the maximum pressure with $\Delta R/R_o$ is linear over the range of shell thicknesses considered. Also, the values of the pressure maxima for material G are about 10% greater than those for material A for all three values of $\Delta R/R_o$.

4.3. Indentation

Indentation calculations, as illustrated in Fig. 2, were carried out for the three values of the shell thickness to outer radius ratio, $\Delta R/R_o$, in Fig. 6. For each thickness, the indentation response was computed for various values of internal pressure, p. For the thinnest shell analyzed, $\Delta R/R_o = 0.05$ the values of p were $p = 0, 1.1, 2.2$ MPa while for $\Delta R/R_o = 0.1$, $p = 0, 2.2, 4.4$ MPa and for $\Delta R/R_o = 0.2$ $p = 0, 4.4, 8.8$ MPa. In addition, for material A with $\Delta R/R_o = 0.2$ calculations were carried out with $p = -4.4$ MPa and $p = -8.8$ MPa.

4.3.1. Shell effect

Indentation into a half-space was modeled in Tvergaard and Needleman (2012) for eight sets of polymer material parameters including those associated with materials A and G. For indentation into a shell, we expect that the indentation hardness will be the same as for a half-space for a sufficiently small indentation depth. At some indentation depth, the effect of the shell geometry will come into play, as the indentation force becomes large enough to deform the shell. In order to explore this transition calculations were carried out for both material A and material G for a shell having a thickness to outer radius ratio $\Delta R/R_o = 0.2$ with $p = 0$. A finite element mesh was used consisting of 240×500 ($r \times \theta$) eight node elements with a fine uniform mesh of 80×100 eight node elements used in a region of depth $0.006 R_o$ and extent $2°$ near the indenter tip so that there are $722,962$ degrees of freedom.

Fig. 7 shows curves of indentation hardness H, versus indentation depth h for materials A and G for $p = 0$ and a thickness to outer radius ratio, $\Delta R/R_o = 0.2$. The indentation hardness H is defined as

$$H = \frac{P}{\pi r_{\mathrm{con}}^2} \tag{19}$$

where r_{con} is the furthest distance from the axis of symmetry with contact between the indenter and the shell. The indentation depth is normalized by the outer radius of the shell R_o.

The plots in Fig. 7 show indentation hardness values for $h/R_o \geq 0.01$. For smaller values of h/R_o not enough elements are in contact with the indenter to reach a steady state value of H. For $0.01 \leq h/R_o \leq 0.04$ The value of the hardness H remains nearly constant for both materials and then the hardness drops with increasing h. For example, at $h/R_o = 0.01$ $H = 123$ MPa for material G and 112 MPa for material A, at $h/R_o = 0.04$ these values of H are 121 MPa and 110 MPa, respectively, while at $h/R_o = 0.06$ these values decrease to 112 MPa and 98 MPa. At the last stages computed, $h/R_o = 0.076$ for material A, H is 64 MPa and at $h/R_o = 0.084$ for material G, H is 86 MPa. The value of the hardness drops further for material A than for material G and the main drops occur in more or less discrete
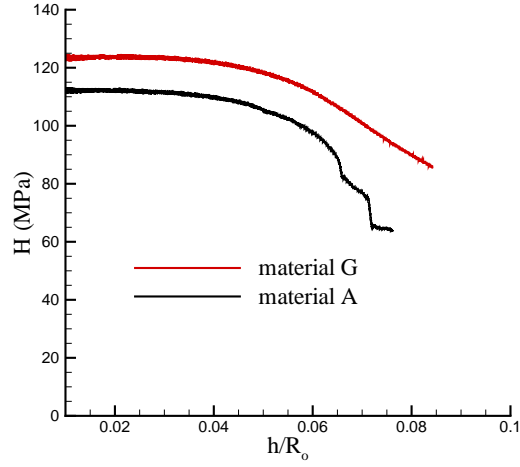
Figure 7: Indentation hardness, H, versus indentation depth, h, for materials A and G with $\Delta R/R_o = 0.2$ and $p = 0$ obtained using a mesh with $722,962$ degrees of freedom.
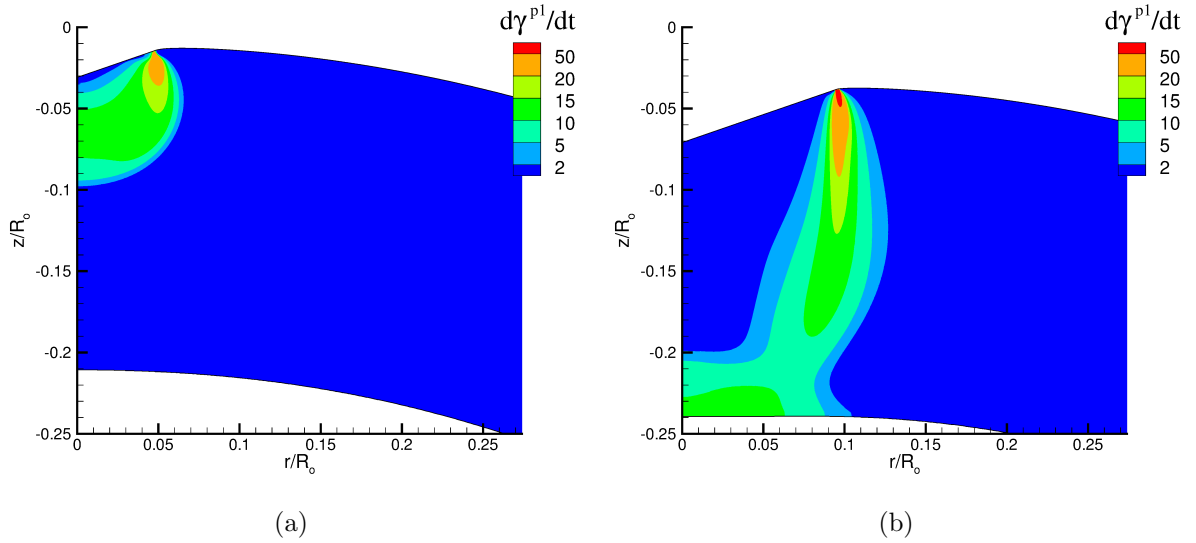

| (a) | (b) |

Figure 8: Distribution of $\dot{\gamma}^{p1}$ in the vicinity of the indenter for material G with $\Delta R/R_o = 0.2$ and $p = 0$. (a) $h/R_o = 0.031$. (b) $h/R_o = 0.071$.

stages. The difference in the evolution of the hardness is associated with the difference in deformation mode for these two materials.

The distributions of plastic strain rate $\dot{\gamma}^{p1}$ in Fig. 8 show the deformation modes for material G at $h/R_o = 0.031$ and $h/R_o = 0.071$. If we normalize the indentation depth with the shell thickness, $h/R_o = 0.031$ and $h/R_o = 0.071$ correspond to $h/\Delta R = 0.093$ and
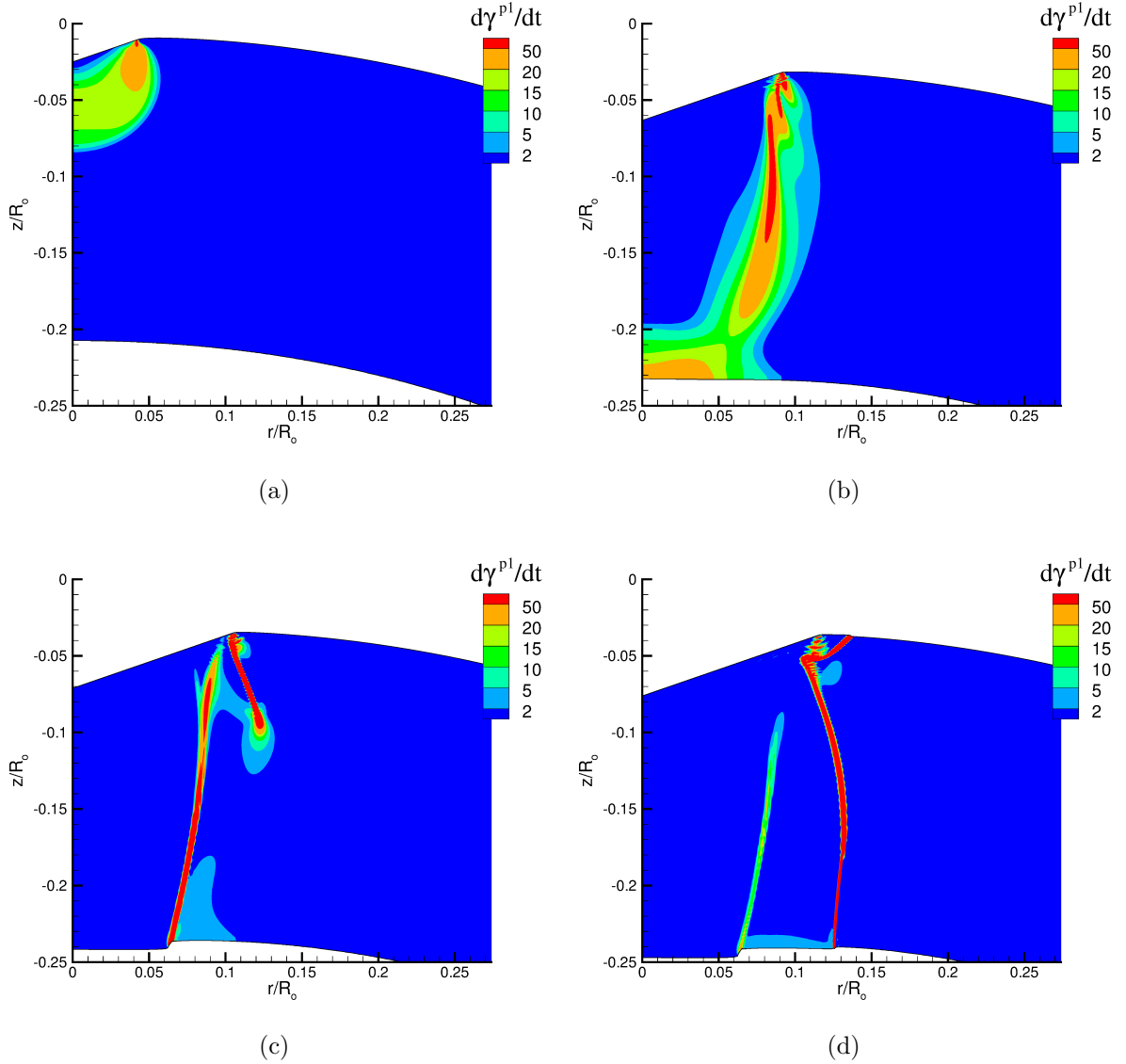
11

Figure 9: Distribution of $\dot{\gamma}^{p1}$ in the vicinity of the indenter for material A with $\Delta R/R_o = 0.2$ and $p = 0$. (a) $h/R_o = 0.025$. (b) $h/R_o = 0.063$ (c) $h/R_o = 0.071$ (d) $h/R_o = 0.076$.

$h/\Delta R = 0.213$. At $h/R_o = 0.031$, the hardness and rate distribution are similar to those for indentation into a half-space. On the other hand, at $h/R_o = 0.071$, the hardness has decreased to 99 MPa, a decrease of about 20%, and the deformation mode has a considerable bending component, partly seen by the deviation of the inner surface from spherical. For material G there is a smooth transition from a pure indentation deformation mode to the one involving bending between $h/\Delta R$ about 0.1 and 0.2.

The evolution of the deformation for material A is quite different as shown in Fig. 9.

12

For a sufficiently small indentation depth, $h/R_o = 0.025$ in Fig. 9a, the deformation mode is similar to that for indentation into a half-space, as is the case for material G. Subsequently, when the plastic strain rate concentration reaches the inner radius, a shell deformation mode involving bending comes into play ($h/R_o = 0.063$, Fig. 9b), again as for material G. Then, because for material A, network stiffening only plays a role at very large strains, the extensive softening results in the emergence of a localized deformation band. The strain rate is concentrated in this band and, as seen in Fig. 9c, it leads to a step on the inner radius. As deformation proceeds and the deformations in this band become very large, deformation shuts down in this band and a second band develops. The development of the localized deformation bands is what gives rise to the rather abrupt drops in hardness for material A with one occurring at $h/R_o \approx 0.06$ and another at $h/R_o \approx 0.07$. It is worth noting that when localization of deformation occurs the mode of deformation deviates significantly from that associated with indentation into a half-space. This is consistent with the lack of occurrence of localization of deformation in the indentation calculations in Tvergaard and Needleman (2011, 2012).

It is worth noting that although the values of H in Fig. 7 for small h/R_o differ for materials G and A, the value of indentation depth h/R_o at which the value of H begins to decrease noticeably is nearly the same for these two sets of material parameters, at about $h/R_o = 0.04$.

It is known that the occurrence of pile-up or sink-in is important for indentation hardness calculations. These effects are fully accounted for in the present computations, which are full finite strain analyses. However, for indentation into a curved surface it is difficult to define sink-in and pile-up. During indentation the surface translates in the indentation direction and does not remain spherical, so the choice of reference surface is not clear. But it is noted that previous analyses for indentation in a half-space (Tvergaard and Needleman, 2011) have shown sink-in. The contact model used in the present analyses, as well as the previous study, is based on assuming sticking contact. Thus, when a surface point has come in contact with the indenter, it translates with the indenter without sliding.

4.3.2. Effect of shell thickness and internal pressure

The calculations exploring the effects of internal pressure p and shell thickness $\Delta R/R_o$ are carried out with fewer elements than those in Section 4.3.1 so that an accurate representation of the indentation deformation fields at small indentation depths is not obtained. Specifically, the calculations in this section with $\Delta R/R_o = 0.2$ were carried out with 20×46 ($r \times \theta$) eight node elements with a fine mesh entirely through the shell thickness (20 elements) and having 24 elements in the interval $90° \geq \theta \geq 75°$.

Fig. 10 compares the hardness H versus normalized indentation depth h/R_o responses obtained with the fine ($722,962$ degrees of freedom) and coarse (5786 degrees of freedom) meshes. The much larger oscillations in the response in the coarse mesh calculations are due to the larger elements coming into contact with the indenter. The mean value of the coarse mesh curves are a bit above those of the fine mesh curves but the overall responses are in rather good agreement, particularly for material G. For material A, the first load drop obtained in the coarse mesh calculation is in fairly good agreement with that of the
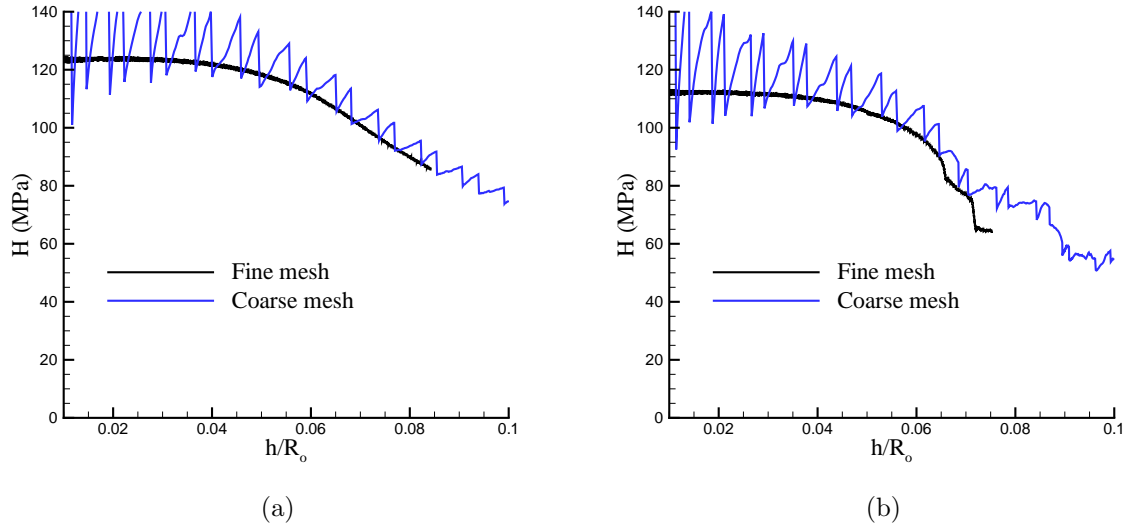
Figure 10: Indentation hardness, H, versus indentation depth, h, with $\Delta R/R_o = 0.2$ and $p = 0$ using a fine mesh ($722,962$ degrees of freedom) and a coarse mesh (5786 degrees of freedom). (a) material G. (b) material A.
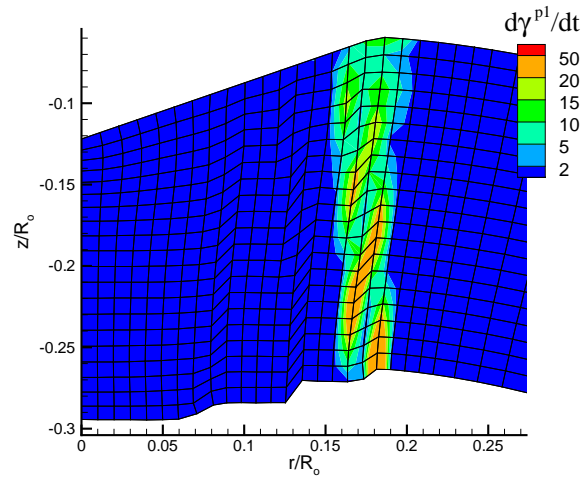

Figure 11: Distribution of $\dot{\gamma}^{p1}$ in the vicinity of the indenter for material A with $\Delta R/R_o = 0.2$ and $p = 0$ at $h/R_o = 0.122$ using the coarse mesh. The deformed mesh is also shown.

fine mesh calculation but the second load drop is significantly delayed.

Fig. 11 shows the distribution of plastic strain rate, $\dot{\gamma}^{p1}$, for material A along with the deformed finite element mesh at the last stage of the coarse mesh calculation, $h/R_o = 0.122$. At this stage of deformation a third shear band is forming. The deformed mesh shows
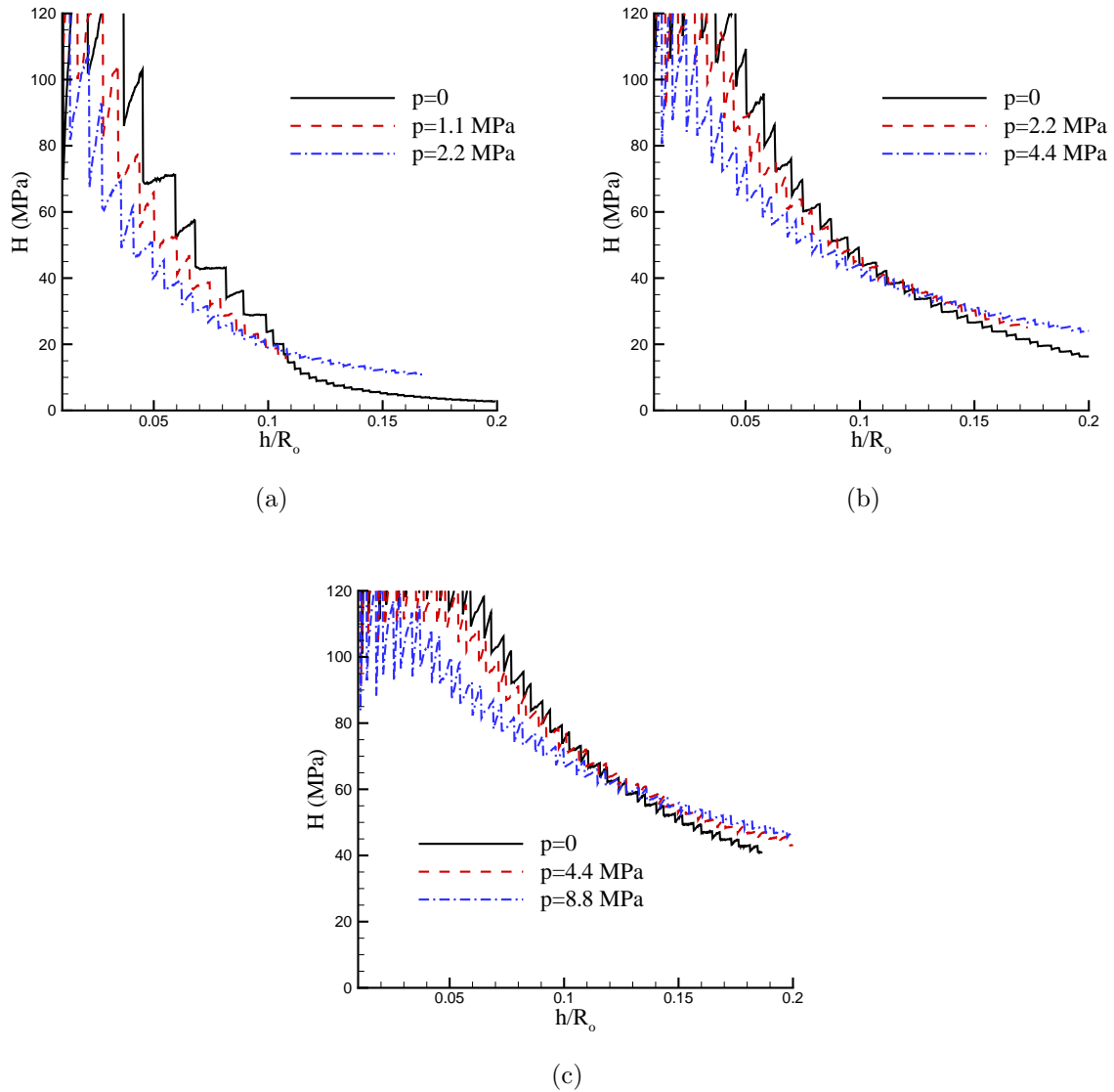
14

Figure 12: Indentation hardness, H, versus indentation depth, h, for material G. (a) $\Delta R/R_o = 0.05$ (b) $\Delta R/R_o = 0.1$ (c) $\Delta R/R_o = 0.2$.

the locations of the first and second shear bands that formed. Comparison with the fine mesh plots in Figs. 9c and 9d shows that the locations where these intersect the inner shell radius are in good agreement. In the coarse mesh calculation, the deformation bands are one element thick. It is worth noting that in the fine mesh calculation the first shear band is two to three elements thick. The second shear band in Fig. 9d is also two to three elements thick through about 2/3 of the the shell thickness and then narrows down to one element thick near the inner radius.
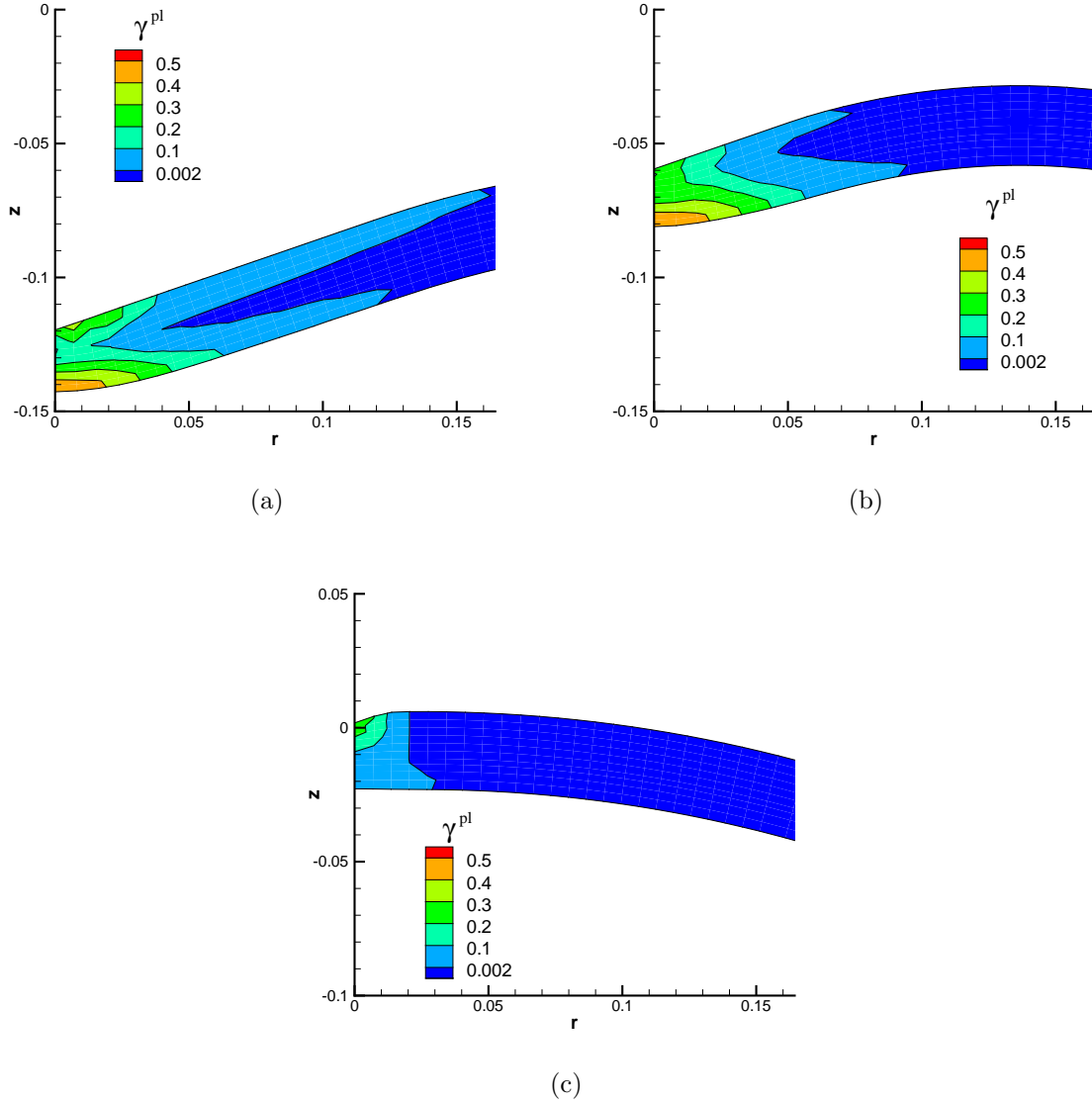
15

Figure 13: Distribution of γ^{pl} in the vicinity of the indenter for material G with $\Delta R/R_o = 0.05$. (a) With $p = 0$ at $h/R_o = 0.20$. (b) With $p = 1.1$ MPa at $h/R_o = 0.11$. (c) With $p = 2.2$ MPa at $h/R_o = 0.17$

Fig. 12 shows curves of indentation hardness, H, versus indentation depth h for material G for three values of the shell thickness to external radius ratio $\Delta R/R_o$. For each value of $\Delta R/R_o$ results are presented for three values of the internal pressure p. The calculations in Fig. 12 were carried out with 2986 degrees of freedom for $\Delta R/R_o = 0.05$, with 4106 degrees of freedom for $\Delta R/R_o = 0.1$ and, as previously noted, with 5786 degrees of freedom for $\Delta R/R_o = 0.2$. With this level of resolution, the oscillations in the indentation hardness H versus indentation depth h/R_o curves dominate in the early stages of deformation. Sub-
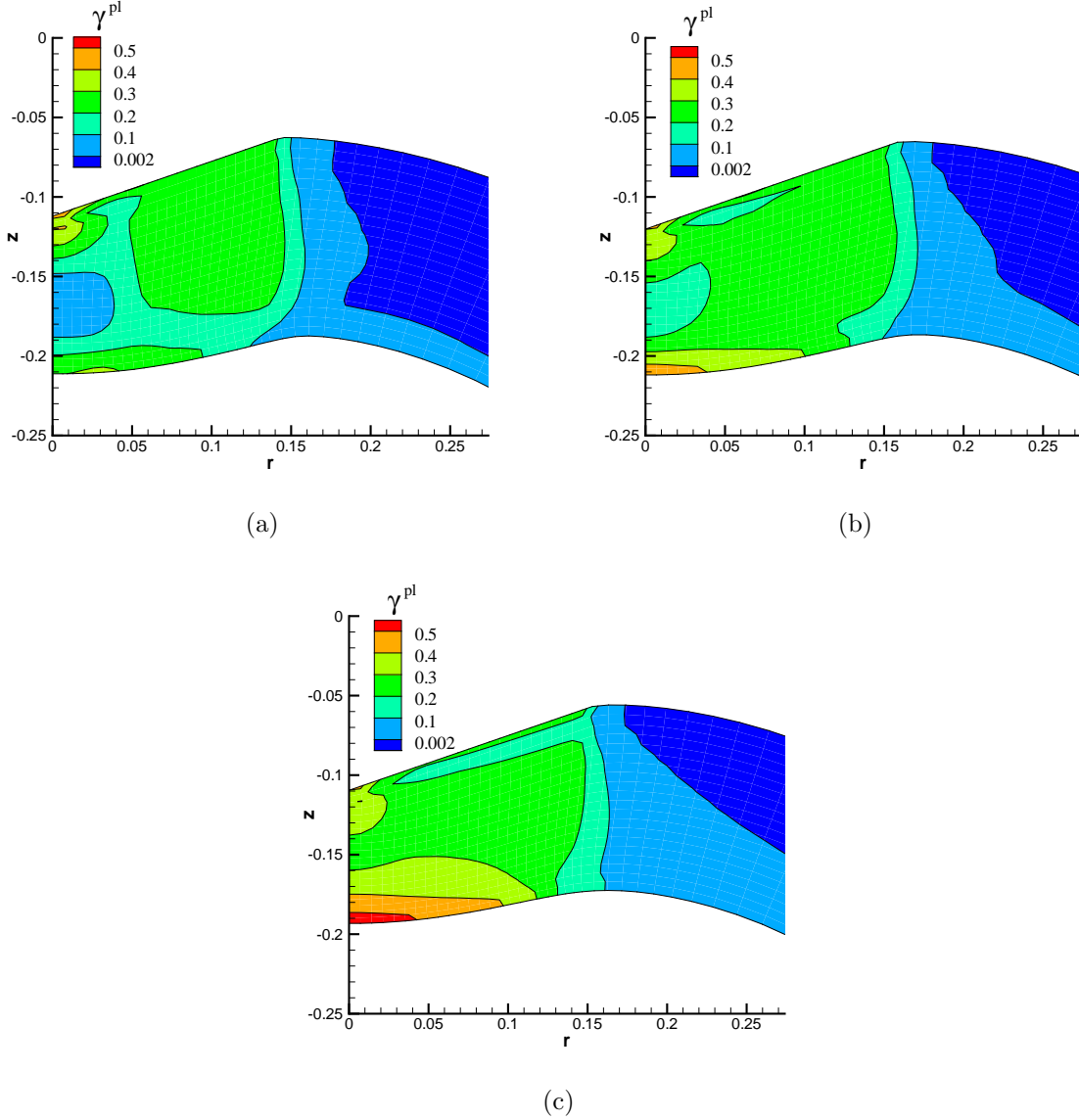
16

Figure 14: Distribution of γ^{pl} in the vicinity of the indenter for material G with $\Delta R/R_o = 0.20$. (a) With $p = 0$ at $h/R_o = 0.19$. (b) With $p = 4.4$ MPa at $h/R_o = 0.21$. (c) With $p = 8.8$ MPa at $h/R_o = 0.20$

sequently, as more elements come into contact with the indenter, the oscillations become much smaller. Presuming that, for fixed material properties, the transition from an indentation dominated deformation mode to one involving considerable bending deformations takes place, at least approximately, at a fixed value of the ratio of indentation depth h to shell thickness ΔR, the transition for $\Delta R/R_o = 0.05$ is expected to occur at about $h/R_o = 0.01$ and at about $h/R_o = 0.02$ for $\Delta R/R_o = 0.1$. Thus, in Fig. 12 when a sufficient number of elements have come into contact with the indenter for the deformation mode to be re-
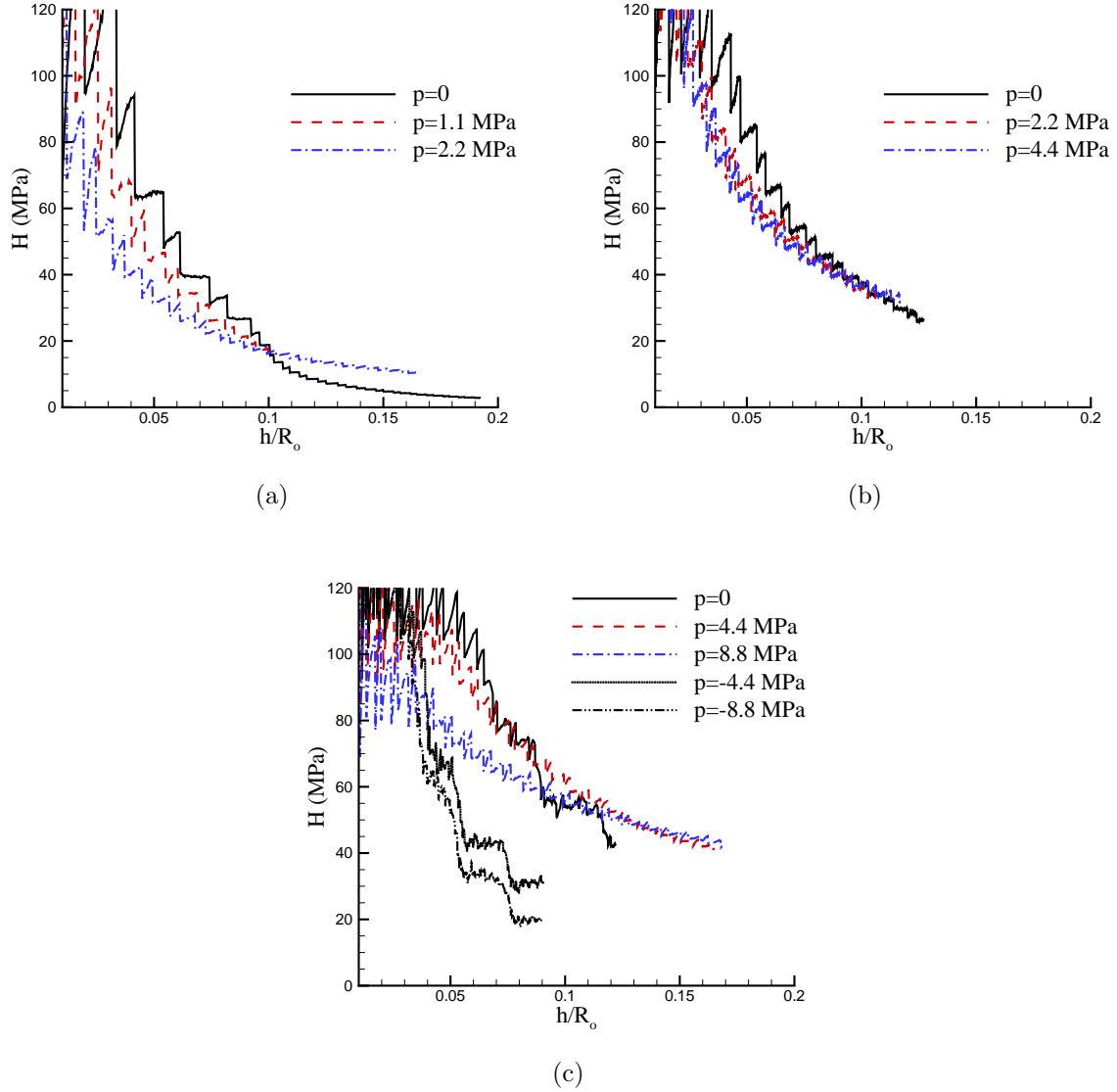
Figure 15: Indentation hardness, H, versus indentation depth, h, for material A. (a) $\Delta R/R_o = 0.05$ (b) $\Delta R/R_o = 0.1$ (c) $\Delta R/R_o = 0.2$.

solved, the bending dominated mode has already developed for these two values of the shell thickness. However, even with the oscillations it is seen in Fig. 12c, where $\Delta R/R_o = 0.2$, that the decrease in indentation hardness H associated with the emergence of the bending dominated deformation mode takes place at about $h/R_o = 0.04$ for all three values of p, as was also seen in Fig. 10a for $p = 0$.

Despite the oscillations it is clear that in the early stages of indentation, the stiffest response is for $p = 0$ whereas in the later stages the softest response is with $p = 0$. The
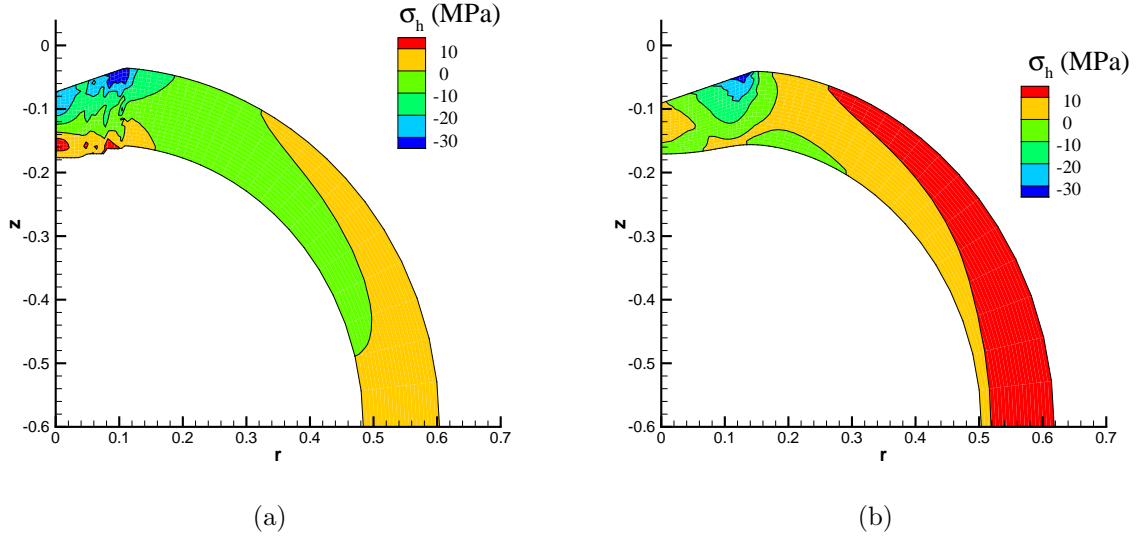
Figure 16: Distribution of σ_h over the region analyzed for material A with $\Delta R/R_o = 0.20$. (a) With $p = 0$ at $h/R_o = 0.12$. (b) With $p = 8.8$ MPa at $h/R_o = 0.17$

reason for this is that during the initial pressurization, the shell material is prestrained so that plastic deformation occurs earlier in the deformation history whereas at large strains the internal pressure induces shell stresses that act to resist bending.

The effect of internal pressure on the plastic strain distribution for material G with $\Delta R/R_o = 0.05$ is shown in Fig. 13 at the last stage of each computation. The largest plastic strains in Figs. 13a and 13b ($p = 0$ and $p = 1.1$ MPa, respectively) are at the inner shell radius indicating a mainly bending mode of deformation. On the other hand, in Fig. 13c, where $p = 2.2$ MPa, the largest plastic strains are near the indented surface.

In Fig. 14, with $h/R_o = 0.2$, the largest values of γ^{p1} are seen in Fig. 14c where $p = 8.8$ MPa. This is a consequence of the more extensive deformation occurring during the shell pressurization phase of the loading. Nevertheless, the lowest value of the indentation hardness still occurs for $p = 0$.

Fig. 15 shows curves of indentation hardness, H, versus indentation depth h for material A for the same values of shell thickness to external radius ratio, $\Delta R/R_o$, and internal pressure p as in Fig. 12. The response in Fig. 15a where $\Delta R/R_o = 0.05$ is similar to that in Fig. 12a in that the case with $p = 0$ gives the largest value of H at a given h/R_o for small values of h/R_o and the smallest value of H for larger values of h/R_o. For $\Delta R/R_o = 0.1$, Fig. 15b, the qualitative nature of the hardness versus indentation depth response is also similar to that obtained for material G in Fig. 12b. However, for material A, the calculations were terminated at a smaller value of h/R_o than for material G. The main difference in the hardness versus indentation depth response between materials A and G occurs for $\Delta R/R_o = 0.2$. In particular, for $p = 0$ the drop in hardness due the localization of deformation is very clear in Fig. 15c. The earlier load drops, signaling localization of deformation, for the cases
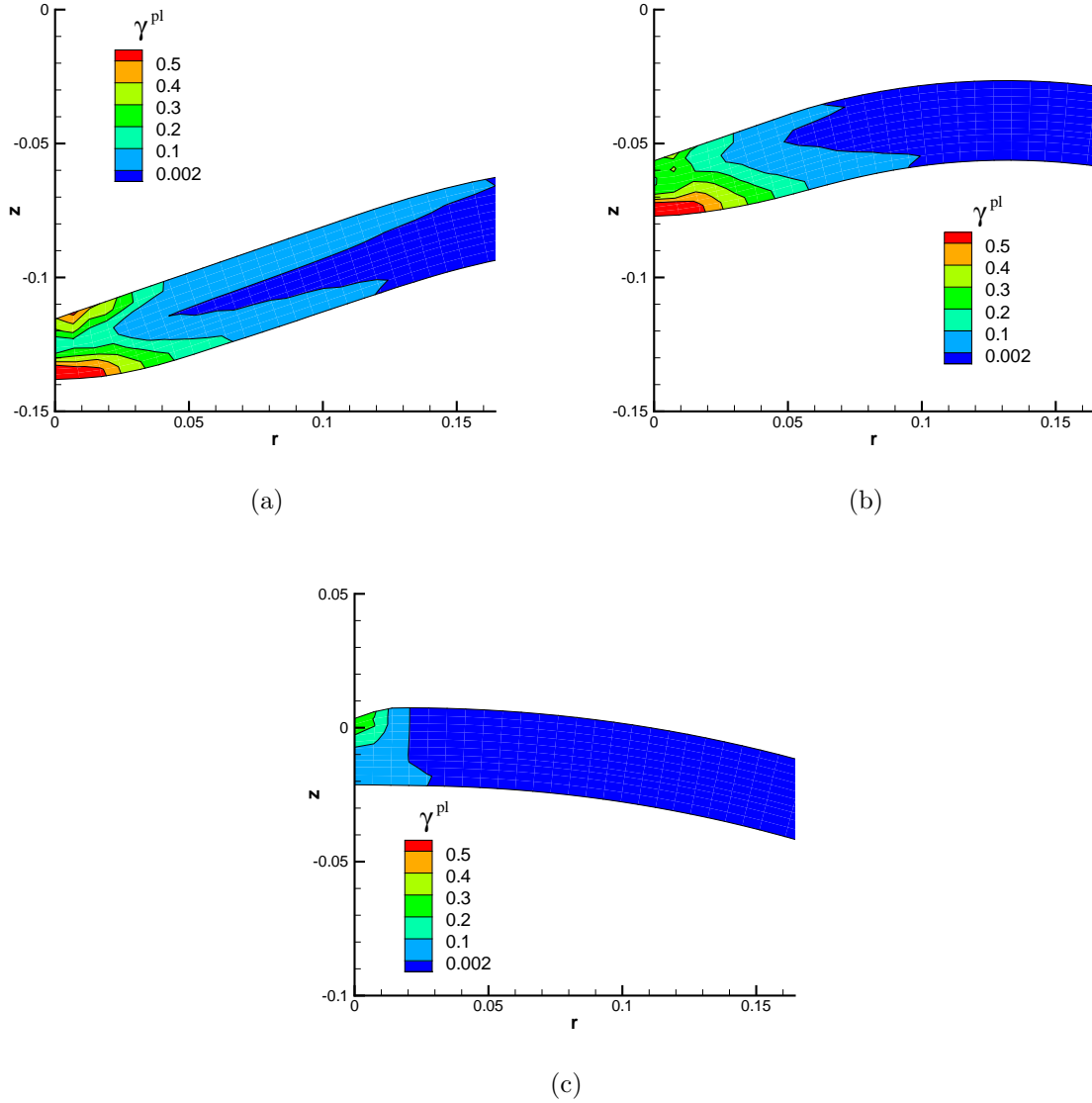
19

Figure 17: Distribution of γ^{pl} in the vicinity of the indenter for material A with $\Delta R/R_o = 0.05$. (a) With $p = 0$ at $h/R_o = 0.19$. (b) With $p = 1.1$ MPa at $h/R_o = 0.10$. (c) With $p = 2.2$ MPa at $h/R_o = 0.17$

with $p = -4.4$ MPa and -8.8 MPa show the strong effect of the compressive shell stresses induced by the negative prescribed pressure on promoting localization.

The distributions of hydrostatic stress, σ_h defined in Eq. (4), in the region analyzed are shown in Fig. 16 for material A with $\Delta R/R_o = 0.2$ and with $p = 0$ and $p = 8.8$ MPa. As seen in Fig. 16(a), with $p = 0$ σ_h, which is the mean value of the principal stresses, is negative over much of the shell whereas σ_h is positive over a large region with $p = 8.8$ MPa in Fig. 16(b).
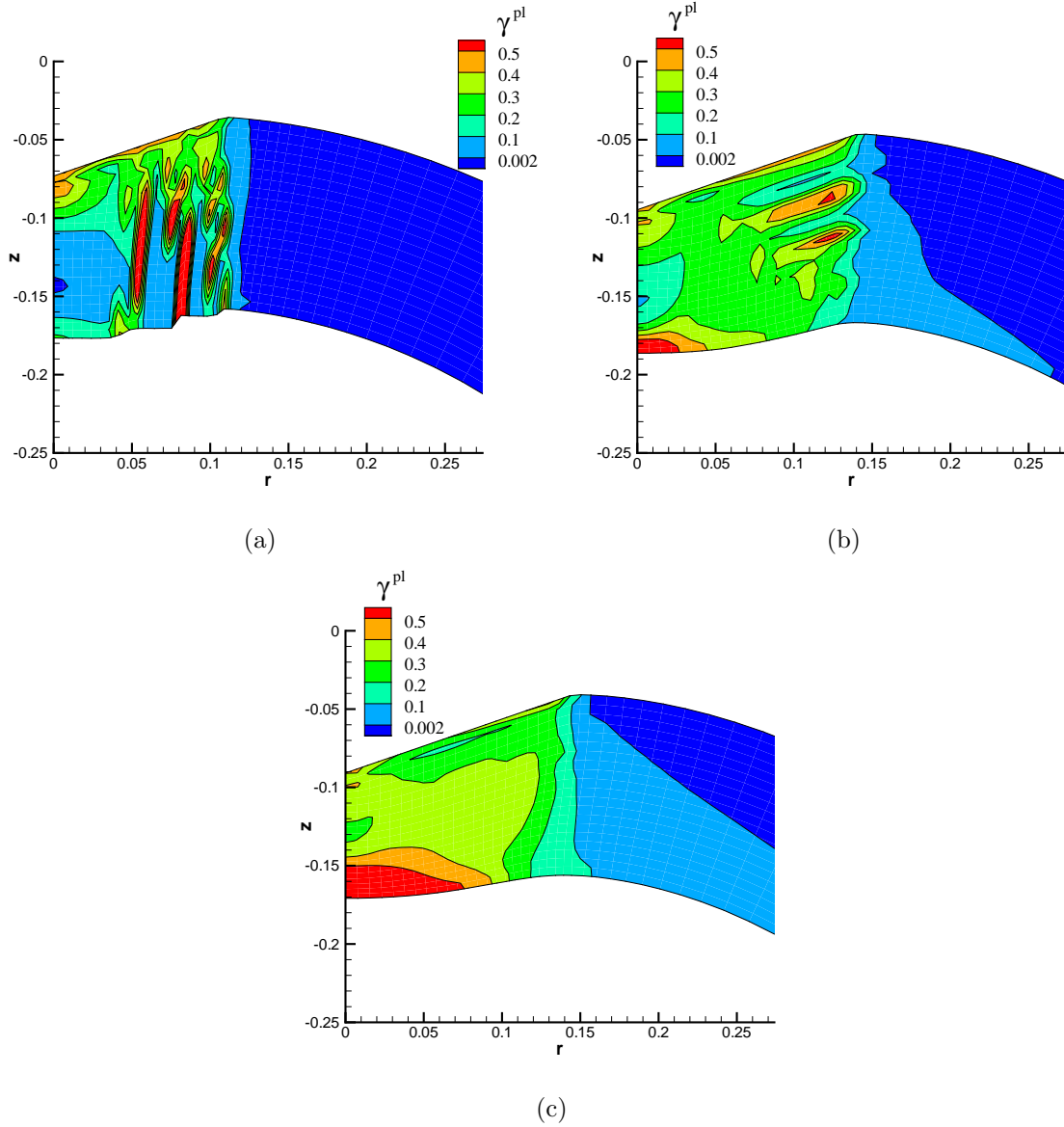
Figure 18: Distribution of γ^{pl} in the vicinity of the indenter for material A with $\Delta R/R_o = 0.20$. (a) With $p = 0$ at $h/R_o = 0.12$. (b) With $p = 4.4$ MPa at $h/R_o = 0.16$. (c) With $p = 8.8$ MPa at $h/R_o = 0.17$

The plastic strain distributions in Fig. 17 show the transition in deformation mode from being essentially bending dominated at low values of the internal pressure to indentation dominated at the largest value of internal pressure computed, $p = 2.2$ MPa. For this thin shell there is no indication of a localized mode of deformation developing over the range computed.

On the other hand, with $\Delta R/R_o = 0.2$ in Fig. 18, as seen previously, with $p = 0$ the deformation mode that develops involves a series of bands of highly localized deformation.
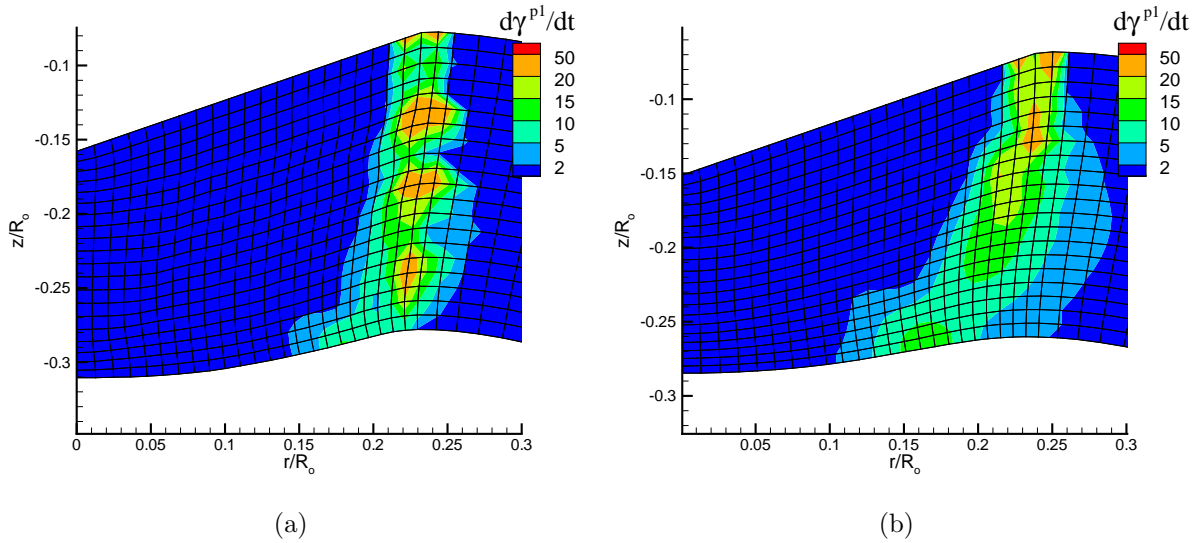
Figure 19: Distribution of $\dot{\gamma}^{pl}$ in the vicinity of the indenter for material A with $\Delta R/R_o = 0.20$. (a) With $p = 4.4$ MPa at $h/R_o = 0.16$. (b) With $p = 8.8$ MPa at $h/R_o = 0.17$

With $p = 4.4$ MPa, there is an indication of a localized deformation mode developing that differs from the one that occurs with $p = 0$. However, with $p = 8.8$ MPa, Fig. 18c, the deformation mode exhibits no tendency to localize, at least over the range of deformations calculated.

The distributions of strain rate for material A with $\Delta R/R_o = 0.2$ in Fig. 19 for $p = 4.4$ MPa and $p = 8.8$ MPa indicate that the bending dominated mode of deformation essential involves deformation in an axisymmetric viscoplastic hinge. This hinge travels away from the axis of symmetry as deformation proceeds. With $p = 0$ in Fig. 11 the deformations localize within the hinge. For $p = 4.4$ MPa and $p = 8.8$ MPa, the internal pressure seems to inhibit the development of localization.

5. Discussion

For the analyses of indentation into a spherical shell the hardness obtained should initially be identical to that for indentation into a half-space, as long as the indentation depth is so small that the resulting indenter force gives only negligible deformation of the shell geometry. The results for the rather thick-walled shell have shown (Fig. 4) that this is a very good approximation as long as the indentation depth is less than about 0.15 times the shell thickness. In this range the plastic zone is limited to a small region around the indenter. However, for larger indents the plastic zone gradually reaches out to the other side of the shell wall, and then deformations of the shell geometry are clearly seen by deviations of the inner shell surface from spherical.

Both of the polymers considered here are prone to localization of plastic flow when the

22

stresses pass the initial sharp peak on the stress strain curve, but for material G an attempt to localize is stopped early on as network stiffening sets in. Then, a band in material G will immediately start to broaden and will not look like a shear band localization. On the other hand, for material A network stiffening occurs at rather large strains and here the results for the thicker shell, $\Delta R/R_o = 0.2$ and $p = 0$, show localized shear bands across the shell wall, both in the analyses using a very fine mesh and in those using a coarser mesh. When a shear band develops near the outer edge of the current indent in material A, this gives a rather sudden reduction of the hardness, i.e. a reduction of the total indenter force. During further indentation the force builds up again until a new shear band develops at the new outer edge of the indent.

The shear band localizations found in the thicker shell for material A are stress state dependent. For no internal pressure there are shear bands, but for the largest internal pressure considered here no shear bands are found. It is noted that the internal pressure results in biaxial tensile hoop stresses in the shell, which are present before indentation starts to give shear stresses in the shell wall. For comparison, analyses were carried out for the same level of negative internal pressure, which gives compressive hoop stresses in the shell. Under these conditions the shell shows an earlier occurrence of shear bands than found for zero internal pressure.

For no internal pressure, as illustrated by the fine mesh calculations in Figs. 7, 8 and 9, there are no hoop stresses resulting from internal pressure. Fig. 9a, for material A, shows a very small indent, where the behavior is similar to indentation in a half-space, but there is no sign of localization. Afterwards, as the hardness H is nearly constant in the beginning, the indentation force P grows approximately in proportion to r_{con}^2, and therefore the average shear stress on a cylindrical cross-section of the shell below the outer edge of the indenter will grow approximately in proportion to r_{con}. At a certain critical level of this shear stress a shear band forms across the shell wall. This relaxes the average shear stress, but after a bit more indentation the shear stress at the larger current r_{con} again reaches the critical level and a new shear band forms, etc. The results show that this shear localization is very sensitive to the stress state resulting from an internal pressure. According to Fig. 15c, these shear bands occur at lower spacing for negative internal pressure, and not at all for positive pressure. It is noted that for material G no shear localization is found at all, since here the strains quickly reach network stiffening in the more deformed broad band (Fig. 8b), which prevents localization.

For the thinnest shell analyzed, $\Delta R/R_o = 0.05$, no shear bands are found, even in the case of material A. Here the much reduced bending stiffness of the shell wall gives reduced indent forces, which will reduce the shear stresses in the wall. For these thin-walled shells the internal pressure gives a dominant contribution to the load carrying capacity. With no internal pressure the thin shells show a large radius of contact with the indenter (Figs. 13a and 17a), while for the largest internal pressure considered the radius of contact with the indenter is much smaller, at about the same value of the indentation depth (Figs. 13c and 17c). For the largest internal pressure considered the thin shells behave more like a balloon, where most of the indentation depth results from general shape changes of the loaded balloon, i.e. a thin shell, see for example Nasto and Reis (2014).

23

Although the indentation response of the shells depends on material properties, shell thickness and the internal pressure, for $p \geq 0$ in both Figs. 12 and 15, the value of the hardness H is nearly independent of p for $h/R_o = 0.1$ for both materials. We will use the value of H at $h/R_o = 0.1$ as an indicator of the scaling with shell thickness. For material G, Fig. 12, the mean values of H for the three values of p with $\Delta R/R_o = 0.05, 0.10$ and 0.20 are 18 MPa, 45 MPa and 72 MPa, respectively. For material A, Fig. 15, the mean values of H with $\Delta R/R_o = 0.2$ (only considering $p \geq 0$ for $\Delta R/R_o = 0.2$) are 17 MPa, 36 MPa and 57 MPa, respectively. Thus, for both material A and material G, the scaling with shell thickness is approximately linear.

The studies for the thin shells analyzed here have some relevance to indentation studies for yeast cells and other natural cells (Vella et al., 2012a; Milani et al., 2011), where the purpose is to get some information on the mechanical properties of the cell wall and the turgor pressure within the cell. Smith et al. (2000) have described yeast compression tests for a Saccharomyces cerevisiae where the thickness to radius ratio is specified as 0.03 to 0.04, i.e. only slightly smaller than the thickness to radius ratio of the thinnest shells analyzed here. Vella et al. (2012a) have proposed using a shallow shell theory as long as indentation gives only small deflections of the cell wall, and for deflections much larger than the shell thickness they have proposed neglecting the bending stiffness so that the shell wall is treated as a membrane where the resistance to indentation results only from the internal pressure combined with the effect of large geometry changes. It is noted that the model used here accounts fully for both small and very large deflections without neglecting the bending stiffness. The model also accounts for the thickness changes and the shear strains, which are present near the tip of the indenter but which are not represented by standard shell theory.

References

Anand, L. and Ames, N.M., 2006. On modeling the micro-indentation response of an amorphous polymer. Int. J. Plast. 22, 1123-1170.

Arruda, E.M., Boyce, M.C. 1993. Evolution of plastic anisotropy in amorphous polymers during finite straining. Int. J. Plast. 9, 697-720.

Bishop, R.F., Hill, R., Mott, N.F., 1945. The theory of indentation and hardness tests. Proceedings of the Physical Society **57** (1945) 147-159.

Boyce, M.C., Parks D.M., Argon, A.S. 1988. Large inelastic deformation of glassy polymers. Part I: rate dependent constitutive model. Mech. Mater. 19, 193-212.

Boyce, M.C., Arruda, E.M. 1990. An experimental and analytical investigation of the large strain compressive and tensile response of glassy polymers. Polym. Engng. Sci. 30, 1288-1298.

Fitch, J.R., Budiansky, B. 1970. Buckling and postbuckling behavior of spherical caps under axisymmetric load. AIAA J., 8, 686-693.

Johnson, K.L., 1970. The correlation of indentation experiments. J. Mech. Phys. Solids 18, 115-126.

Johnson, K.L., 1985. Contact Mechanics. Cambridge University Press, Cambridge.

Kol, A., Gladnikoff, M., Barlam, D., Shneck, R.Z., Rein, A., Rousso, I., 2006. Mechanical properties of murine leukemia virus particles: effect of maturation. Biophys. J., 91, 967-774.

Morris, A.J., Calladine, C.R., 1971. Simple upper bound calcuations for the indentation of cylindrical shells. Int. J. Mech. Sci., 13, 331-343.

Milani, P., Gholamirad, M., Traas, J., Arnéodo, A., Boudaoud, A., Argoul, F., Hamant O., 2011. In vivo analysis of local wall stiffness at the shoot apical meristem in Arabidopsis using atomic force microscopy. Plant J., 67, 1116-1123.

Mulliken, A.D., Boyce, M.C., 2006. Mechanics of the rate-dependent elastic-plastic deformation of glassy polymers from low to high strain rates. Int. J. Solids Struct. 43, 1331-1356.

Needleman, A., Tvergaard, V., Van der Giessen, E., 2015. Indentation of elastically soft and plastically compressible solids. Acta. Mech. Sinica, in press.

Nasto, A., Reis, P.M., 2014. Localized structures in indented shells: a numerical investigation. J. Appl. Mech., 81, 12108.

Ogbonna, N., Needleman, A., 2011. Conical indentation of thick elastic spherical shells. J. Mech. Mater. Struct., 6, 443-452.

Rice, J.R., 1977. The localization of plastic deformation. in Koiter, W.T. (ed.), Proceedings of the 14th International Congress on Theoretical and Applied Mechanics, Delft, North-Holland, pp. 207-220.

Smith, A.E., Zhang, Z., Thomas, C.R., Moxham, K.E., Middelberg, A.P.J., 2000. The mechanical properties of Saccharomyces cerevisiae. Proc. Nat. Acad. Sci., 97, 9871-9874.

Tvergaard, V., Needleman, A., 2011. Polymer indentation: numerical analysis and comparison with a spherical cavity model. J. Mech. Phys. Solids 59, 1669-1684.

Tvergaard, V., Needleman, A., 2012. Effect of viscoplastic material parameters on polymer indentation. Model. Simul. in Mater. Sci. Engin. 20, 065002.

Vaziri, A., Mahadevan, L., 2008. Localized and extended deformations of elastic shells. Proc. Natl. Acad. Sci., 105, 79137918.

Vella, D., A. Ajdari, A., Vaziri, A., Boudaoud A., 2012. The indentation of pressurized elastic shells: from polymeric capsules to yeast cells. J. Roy. Soc. Interf., 9, 448-455.

Vella, D., Ajdari, A., Vaziri, A., Boudaoud A., 2012. Indentation of ellipsoidal and cylindrical elastic shells. Phys. Rev. Lett., 109, 144302.

Wu, P.D., Van der Giessen, E. 1996. Computational aspects of localized deformations in amorphous glassy polymers. Eur. J. Mech. A/Solids 15, 799-823.

Zelenskaya, A., de Monvel, J.B., Pesen, D., Radmacher, M., Hoh, J.H., Ulfendahl, M., 2005. Evidence for a Highly Elastic Shell-Core Organization of Cochlear Outer Hair Cells by Local Membrane Indentation. Biophys. J., 88, 2982-2993.